The Astrophysical Journal, 982:168 (11pp), 2025 April 1 https://doi.org/10.3847/1538-4357/adb8e0

Exploring Unusual High-frequency Eclipses in MSP J1908+2105

Ankita Ghosh[1], Bhaswati Bhattacharyya[1], Sangita Kumari[1], Simon Johnston[2], Patrick Weltevrede[3], and Jayanta Roy[1]
[1] National Centre For Radio Astrophysics, Tata Institute of Fundamental Research, Pune 411007, India
[2] CSIRO Astronomy and Space Science, P.O. Box 76, Epping, NSW 1710, Australia
[3] Jodrell Bank Centre for Astrophysics, Department of Physics and Astronomy, The University of Manchester, UK
Received 2024 November 22; revised 2025 February 15; accepted 2025 February 16; published 2025 March 27

Abstract

This paper presents a comprehensive study of the eclipse properties of the spider millisecond pulsar (MSP) J1908+2105, using wide-band observations from the uGMRT and Parkes UWL. For the first time, we observed that this pulsar exhibits extended eclipses up to 4 GHz, the highest frequency band of the Parkes Ultra-Wideband, making it one of only three MSPs known to have such high-frequency eclipses. This study reveals synchrotron absorption as the primary eclipse mechanism for J1908+2105. We present modeling of synchrotron optical depth with various possible combinations of the parameters to explain the observed eclipsing in this as well as other spider MSPs. Observed eclipses at unusually high frequencies for J1908+2105 significantly aided in constraining the magnetic field and electron column density in the eclipse medium while modeling the synchrotron optical depth. Combining our findings with data from other MSPs in the literature, for the first time we note that a higher cutoff frequency of eclipsing, particularly above 1 GHz, is consistently associated with a higher electron column density ($>10^{17}$ cm^{-2}) in the eclipse medium. Additionally, we present the first evidence of lensing effects near eclipse boundaries in this MSP, leading to significant magnification of radio emissions. The orbital-phase-resolved polarization analysis presented in this paper further indicates variation in rotation measure and consequently stronger magnetic fields in the eclipse region.

Unified Astronomy Thesaurus concepts: Binary pulsars (153); Millisecond pulsars (1062)

1. Introduction

Millisecond pulsars (MSPs) in compact binary orbits having a low-mass nondegenerate or partially nondegenerate companion with an orbital period of less than a day are known as "spider MSPs" (M. S. E. Roberts 2013). Depending on the mass of the companion (M_c), these spider MSPs are further divided into two categories; "black widow (BW)" ($M_c < 0.05\,M_\odot$) and "redback (RB)" ($0.1\,M_\odot < M_c < 0.9\,M_\odot$) spiders. As the pulsar and the companion are in very close proximity, in these systems, the highly energetic wind from the pulsar ablates the companion. Material blown from the companion causes an eclipse by obscuring the pulsar's radio emission. Frequency-dependent eclipsing is reported for a majority of known spider MSPs. Such eclipsing MSP systems can aid in the understanding of properties of the low-mass companions in tight binary orbits, plasma properties of eclipse material, mass flow from the companion driven by relativistic pulsar wind, orbital properties in strong gravitational potential, etc. C. Thompson et al. (1994) reviewed a set of plausible eclipse mechanisms suggested by several authors. The majority of these works proposed cyclo-synchrotron absorption as a likely eclipse mechanism for low-frequency eclipses and scattering/stimulated Raman scattering as the cause of high-frequency eclipses. Understanding the eclipse mechanism allows us to investigate the subsequent properties of eclipsing materials as well as the interpretation of the intrabinary shock that happens in these systems as a result of stellar wind and relativistic pulsar wind interaction.

Polarization properties are closely tied to the local environment of a pulsar, making polarization studies of the eclipse medium in spider MSPs crucial for uncovering the mysteries of the eclipse mechanism (E. J. Polzin et al. 2019). Spider MSPs are particularly intriguing because tracking the evolution of rotational measure (RM) and polarization position angle (PPA) swings throughout the orbit can provide insights into the dynamic state of the ablated material in the eclipse medium. Analyzing the polarization of these pulsars reveals a substantial magnetic field within the eclipse medium, suggesting possible cyclo-synchrotron absorption. Recent polarization studies and plasma-lensing predictions at eclipse ingress and egress (D. Li et al. 2019; E. J. Polzin et al. 2019; K. Crowter et al. 2020) support this, with D. Li et al. (2019) showing how magnetic fields cause different magnifications in time and frequency for the two circular polarizations.

Motivated by this, we present the eclipse and polarization properties of spider pulsar PSR J1908+2105 using the observations from the Giant Metrewave Radio Telescope (GMRT) and Parkes radio telescope (Table 1). PSR J1908+2105 was discovered by searching for radio pulsations targeted toward the unidentified Fermi-Large Area Telescope source with the 327 MHz receiver of the Arecibo (H. T. Cromartie et al. 2016). It has a spin period of 2.56 ms and a dispersion measure (DM) of 61.9067 pc cm^{-3}, with a flux density of 0.6 mJy at 327 MHz. J. S. Deneva et al. (2021) performed a timing analysis of this spider pulsar, revealing that it has an orbital period of 3.51 hr and a minimum companion mass of $0.055\,M_\odot$, placing it between BWs and RBs in the orbital-period-versus-companion-mass space. PSR J1908+2105 also exhibits unique characteristics, sharing properties from both BWs and RB spiders similar to another such system J1242−4712 (A. Ghosh et al. 2024), suggesting a category of objects that share properties bridging these two subclasses of spider binary systems. Given the rarity of

Table 1
Summary of Observations

Backend	T_{res} [a] (μs)	F_{res} [b] (MHz)	Bandwidth (MHz)	Center Frequency (MHz)	No. of Epochs
Parkes UWL	5.189	1.0	3328	2368	2
uGMRT	10.24	0.39	200	400	3
uGMRT	10.24	0.39	200	650	2

Notes.
[a] Time resolution.
[b] Frequency resolution.

such systems, a detailed study is essential to explore the potential evolutionary transition from RBs to BWs. For J1908+2105, the system's short orbital period and relatively small companion mass align with characteristics typical of BW pulsars, whereas the observed extended eclipses are typical characteristics of RB pulsars. J. S. Deneva et al. (2021) suggested the presence of an unusual companion size or a dense plasma distribution surrounding the companion as the possible reason for the extended eclipse in PSR J1908+2105. The eclipse mechanism and polarization properties of this system have not been explored. In this paper, we aim to constrain the magnetic field in the eclipse medium by thoroughly investigating the eclipse properties using wide-bandwidth polar observations.

Our observations and analysis methods for this paper are described in Section 2. In Section 3, we investigate how the pulsar's eclipse and polarization properties vary as functions of orbital phase. We discuss the possible eclipse eclipse mechanism in Section 4 and present the conclusions in Section 5.

2. Observations and Data Analysis

We observed PSR J1908+2105 with the uGMRT (G. Swarup 1991; Y. Gupta et al. 2017; S. H. Reddy et al. 2017) in band 3 (300–500 MHz) and band 4 (550–750 MHz) in several epochs as listed in Table 2. The data were coherently dedispersed across each frequency sub-band of 390 kHz using a DM of 61.9067 pc cm^{-3}. We recorded data at a rate of 48 MB s^{-1}, employing 8 bit sampling, and used 512 channels with a sampling time of 10.24 μs. To effectively mitigate the impact of narrowband and short-duration broadband radio frequency interference (RFI), we used RFI mitigation software in conjunction with the GMRT pulsar tool (gptool[4]). To eliminate interchannel smearing, we performed incoherent dedispersion to the obtained filter banks. Then to obtain the folded profile from each epoch's observations, we used the PRESTO task "PREPFOLD" to fold each data set using the parameter file of the pulsar.

We observed PSR J1908+2105 using the Parkes Ultra-Wideband (UWL) receiver (G. Hobbs et al. 2020) in two epochs, 2023 October 21 and 31. The observational frequency range spans from 704 to 4032 MHz, divided into 3328 channels with a frequency resolution of 1 MHz. The data were then coherently dedispersed and folded using the topocentric periodicity of the pulsar. The folded data were organized into subintegrations of duration of 30 s with 1024 phase bins per pulsar period. Observations have a duration of approx 2.5 hr, covering nearly one full orbit of the pulsar. Table 1 provides a summary of these observations.

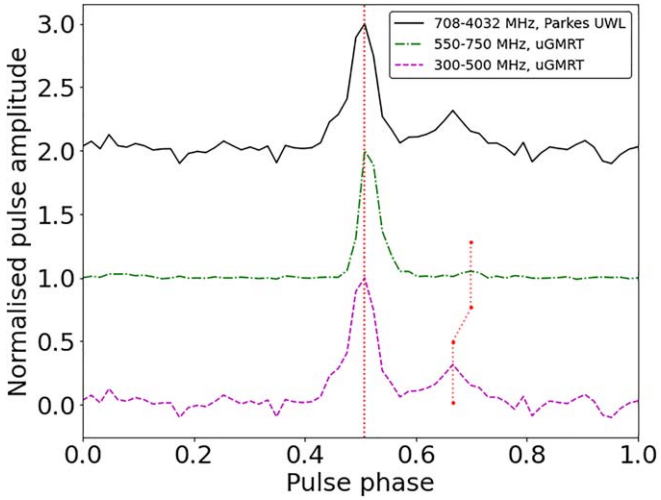

Figure 1. Normalized averaged pulse profiles in the noneclipse region from coherently dedispersed GMRT observation at 400 MHz (dashed magenta line) and 650 MHz (dashed–dotted green line) and Parkes UWL observations at 2368 MHz (solid black line). The vertical dotted line is a visual guide to show how the main peaks at various frequencies are intrinsically aligned. The inflections in the red dotted line indicate shifts in the relative position of the components at higher frequencies.

Before observing the target source, we briefly monitored a pulsed calibration signal injected into the low-noise amplifiers. We used the pipeline PSRPYPE[5] for RFI mitigation. The remaining RFI was manually mitigated in the time and frequency domain. PSRCHIVE (A. W. Hotan et al. 2004) was used for the data processing. The routine "PAC" corrects for instrumental gain and phase differences using the pulsed calibrator, carries out flux calibration obtained from observations of PKS B1934–68, and corrects for instrumental leakage terms using the polarimetric calibration modeling (W. van Straten 2004) method. To improve the signal-to-noise ratio (SNR), we averaged across frequency and phase bins by factors of 8. The end result is a calibrated folded profile comprising 4 Stokes parameters, 416 frequency channels, and 128 phase bins for each epoch. Consecutive observations excluding the eclipse region were combined using the task "PSRADD," generating a single output file. A time drift observed in the combined file was rectified by updating the pulsar ephemeris. This involved fitting the time of arrivals (TOAs) calculated using "PAT," solely for spin frequency (F0), the epoch of ascending node (T0), and projected semimajor axis (A1) using TEMPO2 (G. B. Hobbs et al. 2006). We used this combined average profile from the noneclipse phase to obtain the average polarization fraction and RM of the pulsar.

3. Results and Interpretations

3.1. Profile Evolution

PSR J1908+2105 shows significant profile evolution as we move toward the higher frequencies. A second component is observed to be present at 400 MHz, which is absent at 2368 MHz (Figure 1). The main component has a width at 50% of the peak intensity (W_{50}) of approximately 0.10 ± 0.02 ms at a frequency of 2368 MHz and 0.17 ± 0.04 ms at 400 MHz, and the W_{50} of the

[4] https://github.com/chowdhuryaditya/gptool

[5] https://github.com/vivekvenkris/psrpype/

Table 2
Temporal Change of Eclipse Boundaries

Backend	Frequency (MHz)	Date of Observations	Eclipse Boundary	Orbital Phase (ϕ_p)
Parkes UWL	2368	2023 Oct 21	egress	$0.34 < \phi_p < 0.45$
		2023 Oct 31	ingress	0.125 ± 0.002
uGMRT	650	2024 Jun 3	ingress	$0.012 < \phi_p < 0.085$
		2024 Jun 3	egress	0.390 ± 0.002
		2024 Jun 14	ingress	0.076 ± 0.002
		2024 Jun 14	egress	0.387 ± 0.002
uGMRT	400	2023 Dec 16	egress	0.475 ± 0.002
		2023 Dec 16	ingress	0.098 ± 0.005
		2023 Dec 16	egress	0.447 ± 0.004
		2024 Feb 4	egress	0.465 ± 0.002

Note. The eclipse boundary was determined where the SNR drops below 4σ.

second component is 0.19 ± 0.04 ms at 400 MHz. In the noneclipse phase, the scattering timescale is calculated to be $\tau = 0.08 \pm 0.04$ ms and 0.05 ± 0.02 ms at 400 MHz and 1200 MHz, respectively, by fitting the pulse profile with a convolution of Gaussian and exponential functions, assuming the thin screen model, whereas the calculated scattering timescale is found to be 0.001 ms at 1200 MHz and 0.06 ms at 400 MHz using the DM model given by N. D. R. Bhat et al. (2004).

3.2. Frequency-dependent Eclipse

In most spider systems, the duration of the eclipse decreases with increasing frequency, and eclipses often disappear entirely above 1.4 GHz. PSR J1908+2105 eclipses for ∼40% of the orbit is at 327 MHz (J. S. Deneva et al. 2021). We found that the eclipse duration is approximately 38% at 400 MHz, reducing to 31% at 650 MHz. At 2368 MHz, we could not precisely probe the egress boundary where the pulse reappears after the eclipse. Assuming a symmetric eclipse and that the eclipse center does not change from our observations on 2023 December 16, we estimate the duration to be around 30% at this frequency. However, as shown in Table 2 and Figure 2, the center of the eclipse at 650 MHz is shifted to the left compared to 400 MHz. This shift may be a temporal effect due to the turbulent nature of the eclipse medium, given the considerable time gap between the observations.

3.3. Electron Density Distribution near Eclipse

PSR J1908+2105 shows an eclipse for approximately 38% of its orbit at 400 MHz. We investigated the orbital phase–dependent DM variation for PSR J1908+2105 and observed an increase in the DM value near the eclipse boundaries. The excess DM and the corresponding electron column density (N_e) as the function of the orbital phase (illustrated in Figure 2) are determined from the delay in the TOA of pulses (obtained using TEMPO2) using the relation

$$\mathrm{DM_{ex}\,(pc\ cm^{-3})} = 2.4 \times 10^{-10} \times \mathrm{TOA\ delay}\,(\mu\mathrm{s}) \times f^2\,(\mathrm{MHz}), \quad (1)$$

where TOA delay is the time delay in μs and f is the observing frequency in MHz. From $\mathrm{DM_{ex}}$, the excess N_e is computed using

$$\mathrm{Excess}\ \ N_e\ (\mathrm{cm^{-2}}) = 3 \times 10^{18} \times \mathrm{DM_{ex}(pc\ cm^{-3})}. \quad (2)$$

We were able to observe the ingress (when the pulsar is entering the eclipse) of the eclipse only during one epoch, while the egress (when the pulsar is coming out of the eclipse) was observed in three epochs using uGMRT band 3 observations. During the ingress of the MSP, the loss of pulsation is very abrupt, whereas during eclipse egress, it gradually decreases, leaving a distinct trail of materials (Figure 2). Table 2 details temporal shifts of eclipse boundaries corresponding to different epochs. For example, The orbital phase at which the pulse reappears at 400 MHz was observed to vary between 0.447 and 0.485, translating to an approximately 8 minute difference. Such variability suggests that the boundary of ablated material around the companion is not sharply defined, causing an unstable and turbulent egress. The eclipse boundaries are determined by observing the SNR of subintegrations near the eclipse region, specifically where the SNR falls below 4.

The e-folding time, as defined in M. F. Ryba & J. H. Taylor (1991) for PSR B1957+20, is the time over which the local column density decreases by a factor of $e \sim 2.718$. At eclipse ingress for J1908+2105, we determined the change in orbital phase corresponding to an e-folding of the local column density to be $\Delta\phi \sim 0.0047$. During this time, the companion star advances in its orbit by about 25,000 km. At eclipse egress, the e-folding length scale is about 3 times larger, corresponding to $\Delta\phi \sim 0.0157$ (Figure 2). During this time, the companion star advances in its orbit by about 86,000 km. This explains the long trail observed near egress caused by the sweeping of the stellar material due to the companion's orbital motion as found by A. S. Fruchter et al. (1988) for PSR B1957+20. The asymmetric distribution of material at either side of the eclipse is also seen for BW PSR B1957+20 (M. F. Ryba & J. H. Taylor 1991; M. Tavani & L. Brookshaw 1991). As noted in E. J. Polzin et al. (2018), magnetic reconnection between the pulsar wind's magnetic field and the companion's magnetosphere can result in eclipse material leaking into the pulsar wind. This process may explain the excess material observed in the eclipse tail as the companion progresses in its orbit. However, whether the tail of excess material appears at egress or ingress depends on the combined influence of gravitational pressure, Coriolis forces, and the relative velocity of the pulsar wind compared to the companion's orbital velocity (M. Tavani & L. Brookshaw 1991). For instance, in the case of PSR J1744–24A, these effects push the eclipse material toward ingress, forming a tail near the ingress boundary, whereas for PSR B1957+20, the material is pushed toward the egress (M. Tavani & L. Brookshaw 1991). This aligns with the two-dimensional smoothed-particle hydrodynamics calculations of eclipse outflow by M. Tavani & L. Brookshaw (1991). At 400 MHz, GMRT observations on 2023 December 16 show $\Delta\mathrm{DM} \sim 0.02\,\mathrm{pc\,cm^{-3}}$ near orbital phase $\phi = 0.48$ during egress. However, moving closer to the companion, at 2368 MHz, Parkes observations on 2023 October 21 show $\Delta\mathrm{DM} \sim 0.6\,\mathrm{pc\,cm^{-3}}$ near $\phi = 0.455$. Therefore, assuming, that the eclipse center did not change between the observations, we can calculate the slope of increase in DM with orbital phase $(\frac{\delta(\Delta\ \mathrm{DM})}{\Delta\phi}) \approx 23\,\mathrm{pc\,cm^{-3}}$. Similarly, during ingress, uGMRT observations show $\Delta\mathrm{DM} \sim 0.013\,\mathrm{pc\,cm^{-3}}$ near $\phi = 0.09$, increasing to $0.18\,\mathrm{pc\,cm^{-3}}$ at 2368 MHz near $\phi = 0.125$ and therefore, the slope of increase in DM with orbital phase $(\frac{\delta(\Delta\ \mathrm{DM})}{\Delta\phi}) \approx 5\,\mathrm{pc\,cm^{-3}}$, indicating a

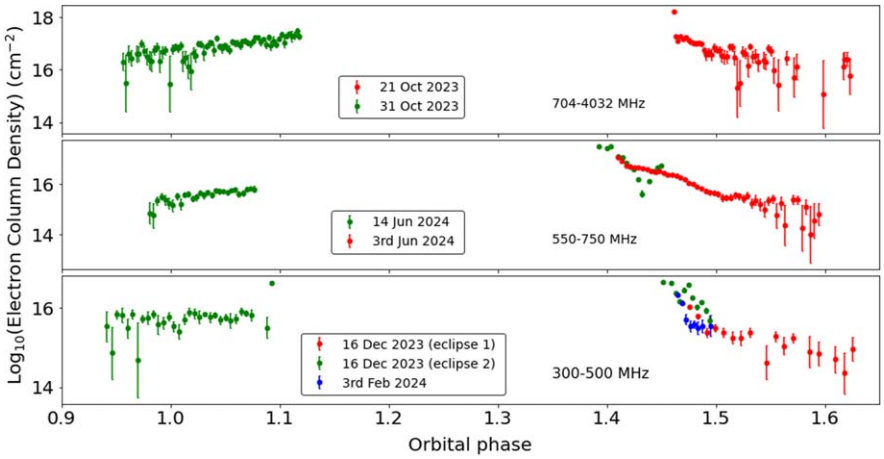

Figure 2. Electron density variation near eclipse boundary in different epochs observed with uGMRT at 400 MHz and 650 MHz and with Parkes UWL at 2368 MHz. A sharp dip around orbital phase ∼1.42 on 2024 June 14 suggests a localized gap in the ionized gas, likely caused by turbulence in the plume. The absence of this dip in data from 11 days earlier indicates variability in timescales of days to weeks.

sharp rise in DM at egress compared to ingress when we move closer toward the companion. Thus, we could predict the possible Δ DM $\sim 4\,\mathrm{pc\,cm^{-3}}$ at the eclipse center ($\phi \sim 0.28$) and corresponding electron column density (N_e) to be $\approx 10^{19}\,\mathrm{cm^{-2}}$. Despite the typical trend of eclipse duration decreasing with frequency, this MSP exhibits an unusually prolonged eclipse, covering over 30% of the orbit even at frequencies up to 4 GHz and likely extending well beyond. Such eclipses at high frequencies are exceedingly rare and, to our knowledge, have been reported for only two other spider MSPs (e.g., PSR J1723−2837 and J1731−1847). The eclipse mechanisms at such high frequencies have not been thoroughly investigated for either of these two MSPs. This necessitates constraining the eclipse mechanism that can account for eclipses occurring even at such high frequencies.

3.4. Orbital-phase-resolved DM and Polarization Properties

We have performed a polarization study on PSR J1908+2105 using our observations from Parkes UWL (708–4032 MHz) only. We have obtained the integrated polarization profile (Figure 3) for J1908+2105 by adding the observations of the noneclipse phase, which are calibrated and RM corrected. We report the best fit RM value is $201 \pm 1\,\mathrm{rad\,m^{-2}}$ from the integrated average profile of the pulsar. The average pulse profile shows linear polarization of nearly 32% in the noneclipse phase. The circular polarization fraction is comparably low at ∼2.8%. We used the full bandwidth of 3328 MHz of the frequency band (708–4032 MHz) to calculate the total intensity and polarization properties. We analyzed the variation of intensity and polarization fraction, as well as RM and DM as a function of the orbital phase. Flux density calculations were done following the method explained in D. Kansabanik et al. (2021). We used TEMPO2 to find the DM variation with the orbital phase. We observed the effect of the eclipse through a decrease in total intensity and linear polarization fraction and an increase in DM and RM around superior conjunction (orbital phase, 0.12–0.40; Figure 4). Where the average RM is $\sim 201\,\mathrm{rad\,m^{-2}}$ for the noneclipse phase, near the eclipse medium, RM increases to $230\,\mathrm{rad\,m^{-2}}$. The increase in DM and RM shows the increased electron density near the eclipse medium. The orbital phase–dependent flux density is calculated

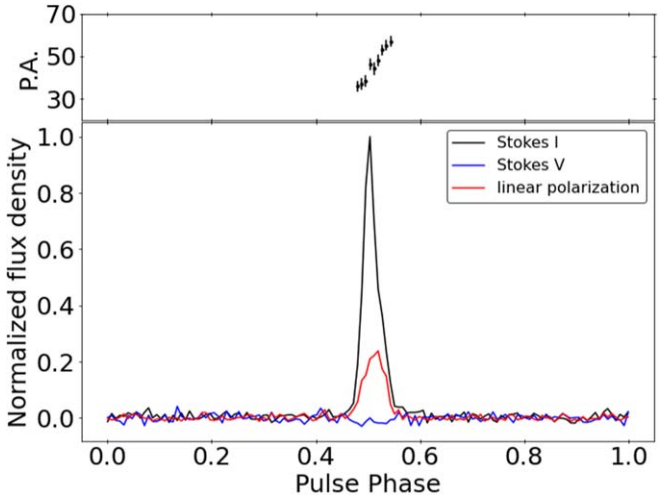

Figure 3. Polarization profile at 2368 MHz from Parkes UWL observations in the noneclipse region. The upper panel shows the PPA variations (in black dots) and RVM fit (in red line) to it.

considering the full bandwidth of the Parkes UWL band, with a central frequency of 2368 MHz and a bandwidth of 3328 MHz.

Depolarization during the eclipse phase has been observed in spider MSPs, for example, PSR J2051–0827 by S. Q. Wang et al. (2023), PSR J2256–1024 by K. Crowter et al. (2020), and J1748–2446A by X. P. You et al. (2018). This depolarization can occur due to the increased RM near eclipse as well as multipath propagation of pulsed radiation through the circumstellar magnetized plasma leading to rapid time variations in the RM. Such rapid RM variations can result from fluctuations in either or both of the circumstellar components of DM and the parallel component of the magnetic field. DM variations are observed at both eclipse ingress and egress for eclipsing spider pulsars. However, these variations are typically very low, which will not significantly affect the RM (X. P. You et al. 2018). We investigated the orbital phase–dependent DM variation for PSR J1908+2105 and observed an increase in the DM value during the eclipse phase (around ∼0.12–0.40), which was, however, not very significant. The excess DM and the corresponding electron column density (N_e) as the function of the orbital phase is illustrated in Figure 4. These maximum DM variations are found to be of the order $\sim 0.07\,\mathrm{pc\,cm^{-3}}$ and

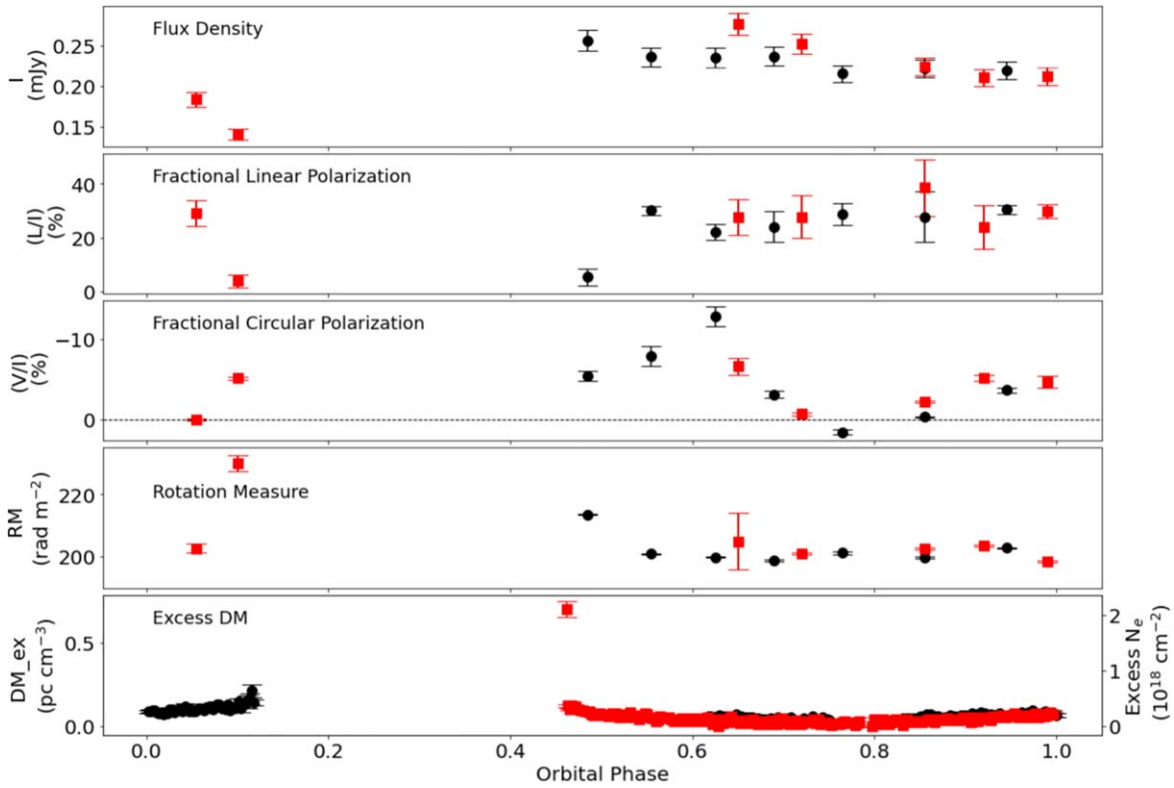

Figure 4. Variation of total intensity and polarization fractions along with RM and DM as a function of orbital phase for PSR J1908+2105 at 2368 MHz from the Parkes UWL observations. Here, each different symbol in a single panel shows observations from different epochs.

0.6 pc cm^{-3} near the ingress and egress boundary, respectively, at the observing frequency of Parkes. Since RM can fluctuate with changes in DM and magnetic field, the small increase in DM observed is unlikely to significantly impact the RM. Therefore, short-timescale variations in the line-of-sight magnetic field can cause depolarization through rapid fluctuations of RM in time, indicating that there might be a significant magnetic field in the eclipse medium, which can also be inferred from the increased RM near the eclipse medium for this MSP. Such fluctuation of the magnetic field is common in the turbulent stellar wind.

3.5. Magnetic Field in the Eclipse Medium

During the ingress of the eclipse, the maximum RM is about 230 rad m^{-2} with a $\Delta \mathrm{RM}_{\mathrm{max}}$ of 30 rad m^{-2} compared to that of the noneclipse phase. The ΔDM at the orbital phase of $\Delta \mathrm{RM}_{\mathrm{max}}$ is 0.05 pc cm^{-3}. The line-of-sight magnetic field strength in the eclipse boundary can be estimated by measuring the changes in the Faraday rotation, $B_{||} = 1.23\ \mu$G $\frac{\Delta \mathrm{RM}}{\Delta \mathrm{DM}} = 0.9$ mG.

Similarly, during the egress of the eclipse, the maximum RM is about 213 rad m^{-2} with a $\Delta \mathrm{RM}_{\mathrm{max}}$ of 13 rad m^{-2} compared to that of the noneclipse phase. The ΔDM at the orbital phase of $\Delta \mathrm{RM}_{\mathrm{max}}$ is 0.017 pc cm^{-3}. The line-of-sight magnetic field strength in the eclipse egress is therefore estimated to be $\sim$1 mG. Since PSR J1908+2105 shows a complete eclipse until 4 GHz, we were not able to obtain the magnetic field in the eclipse center through RM variation. Therefore, for the center of eclipse medium, we calculated the characteristic magnetic field (B_E), using the pressure balance between pulsar wind energy density ($\mathrm{U}_E = \frac{\dot{E}}{4\pi c a^2}$) and the stellar wind energy density of the companion ($\frac{B_E}{8\pi}$), where a is the distance between the pulsar and the companion ($a \sim 1.30\, R_\odot$) and c is the speed of light. This gives the characteristic magnetic field for PSR J1908+2105 to be $\sim$16 G in the center of the eclipse medium. There have been efforts to constrain the magnetic fields of several other spider pulsars. For instance, S. Q. Wang et al. (2023) estimated the magnetic field for J2051–0827 to be 0.1 G at the eclipse boundary from the observed RM variation. E. J. Polzin et al. (2019) analyzed the polarization properties of PSR J2051–0827, providing tentative constraints on the line-of-sight magnetic field (20 $\pm$ 120 G) and the (near-) perpendicular field (<0.3 G) inside the eclipse medium. K. Crowter et al. (2020) derived the magnetic field for PSR J2256–1024 from RM variations near the eclipse boundary, suggesting a line-of-sight magnetic field strength of approximately 1.11 mG at the eclipse boundary. D. Li et al. (2019) constrained the line-of-sight magnetic field ($B_{||}$) and its spatial structure (σB) using plasma lensing, finding the line-of-sight magnetic field strength near the eclipse boundary of PSR B1957+20 to be less than 0.02 G. Additionally, F. X. Lin et al. (2023) detected evidence of Faraday conversion and attenuation in PSR B1744–24A, estimating the magnetic field in the eclipse medium to be approximately 100 G.

3.6. Constraining the Emission Geometry

The PPA in the noneclipse medium showed a hint of swing over the pulse profile. We have explored the rotating vector model (RVM, defined in Equation (3); V. Radhakrishnan & D. J. Cooke 1969) to fit the swing and constrain the emission

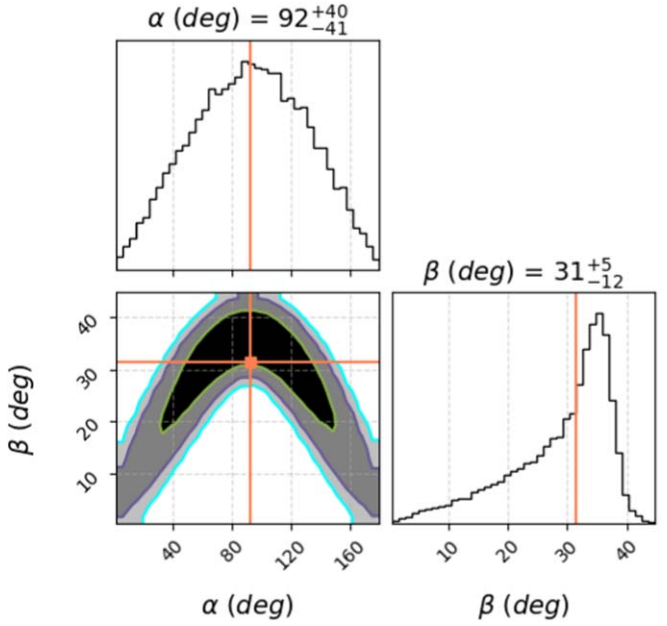

Figure 5. Posterior distribution of RVM fit.

geometry:

$$\tan(\psi - \psi_0) = \frac{\sin\alpha \sin(\phi - \phi_0)}{\sin(\alpha+\beta)\cos\alpha - \cos(\alpha+\beta)\sin\alpha\cos(\phi-\phi_0)}. \quad (3)$$

ϕ represents the pulsar's rotation phase, while α and β are the magnetic latitude and sightline impact angle, respectively. ψ_0 and ϕ_0 represent the offsets in PPA and magnetic latitude. Since ψ_0 corresponds to the position angle at the steepest gradient point in the PPA swing, we estimated the offsets by maximizing the rate of change of the PPA. Our derived ψ_0 and ϕ_0 values are 34° and 176°, respectively. We then used Markov Chain Monte Carlo to explore the posterior distributions of α and β. The median values with 1σ errors of the posterior distributions for α and β are $92^{\circ}_{-41^{\circ}}{}^{+40^{\circ}}$ and $31^{\circ}_{-12^{\circ}}{}^{+5^{\circ}}$, respectively. The banana-shaped joint posterior distribution (Figure 5) indicates the intrinsic degeneracy of the angles in the fitted model.

3.7. Mass Loss

Following the assumptions by C. Thompson et al. (1994), we consider material flowing radially outward from the companion within the eclipse region, confined to an approximately spherical region centered on the companion with a diameter equal to the eclipse width, $2R_E$, where R_E is the eclipse radius. This material initially leaves the companion's surface at escape velocity, which is significantly lower than the pulsar wind velocity (V_W), and is thus carried away by the pulsar wind with velocity V_W. Therefore, the mass-loss rate from the companion can be estimated as, $\dot{M}_c \sim \pi R_E^2 n_e m_p V_W$. If the momentum flux of the ablated material is taken to be equal to the momentum flux of the pulsar wind at the distance of the companion, then $V_W = (U_E/n_e m_p)^{1/2}$. Assuming the pulsar wind to be isotropic, then we find the energy density of the wind at the companion distance, $U_E = (\frac{\dot{E}}{4\pi c a^2})$, where $\dot{E} = \frac{4\pi^2 I\dot{P}}{P^3}$ is the spin-down energy loss rate of the pulsar and $a = a_p + a_c$ is the orbital separation between the pulsar and the companion, where, $a_p \sin i$, the projected semimajor axis of pulsar orbit, $= 0.116895$ lt-s (J. S. Deneva et al. 2021) and a_c, the semimajor axis of the companion's orbit, $= a_p M_{\rm psr}/M_c$.

For PSR J1908+2105, $\dot{E}$ is estimated to be approximately $6 \times 10^{35}\,{\rm erg\,s^{-1}}$, assuming a pulsar moment of inertia of $I = 10^{45}\,{\rm g\,cm^2}$ and a separation of about $1.30\,R_\odot$, with an inclination angle (i) of 90°.

At 400 MHz, the eclipse width, $\Delta\phi \sim 0.38$, based on the orbital phase coverage during the eclipse (see Table 2). From the DM distribution discussed earlier, we estimate the electron column density near the egress to be $\sim 8 \times 10^{16}\,{\rm cm^{-2}}$ (Equation (2)). This gives an electron volume density of approximately $4 \times 10^5\,{\rm cm^{-3}}$, leading to an estimated mass-loss rate from the companion of $\dot{M}_c \sim 6 \times 10^{-12}\,M_\odot\,{\rm yr^{-1}}$.

At 650 MHz, the eclipse width is reduced to about $\Delta\phi \sim 0.31$, with an electron column density near the egress of $\sim 1.17 \times 10^{17}\,{\rm cm^{-2}}$. The corresponding electron volume density is approximately $7 \times 10^5\,{\rm cm^{-3}}$, and the estimated mass-loss rate is $\dot{M}_c \sim 5.4 \times 10^{-12}\,M_\odot\,{\rm yr^{-1}}$.

At 2368 MHz, the eclipse width is further reduced to around $\Delta\phi \sim 0.27$, and the electron column density near the egress is $\sim 1.8 \times 10^{18}\,{\rm cm^{-2}}$. This results in an electron volume density of approximately $1.1 \times 10^7\,{\rm cm^{-3}}$, with an estimated mass-loss rate of $\dot{M}_c \sim 2 \times 10^{-11}\,M_\odot\,{\rm yr^{-1}}$.

With the mass-loss rate at 2368 MHz, the companion can completely evaporate in a 3 Gyr timescale. However, as mentioned by E. J. Polzin et al. (2018), long-term orbital dynamics will likely affect the evolution of mass loss. If the magnetic braking of the companion and gravitational radiation are negligible, the mass loss will cause the companion to move far away from the pulsar. Combined with the pulsar's spin-down, this decreased irradiation of the companion star over time is expected to reduce the likelihood of complete evaporation.

3.8. Orbital-phase-resolved Flux Density and Plasma Lensing

The total intensity versus orbital phase is shown in Figure 6 for observations at 400 MHz, and the first panel of Figure 4 shows the flux density variation at 2368 MHz. Similar to PSR J2051−0827 (F. X. Lin et al. 2021), we have seen an enhanced flux density and increase in brightness in pulsed radiation near the first eclipse boundary ($\phi \sim 0.45$–0.60) on epoch 2023 December 16, as shown in Figure 6. The flux density during the eclipse phase of the first eclipse is about 4 times greater than the flux density observed during the noneclipse phase. Additionally, single bright pulses were detected just before and after the radio eclipse, particularly with a high occurrence during the egress of the first eclipse. However, no such bright pulses were detected in the noneclipse region. To determine if this magnification is due to scintillation from the interstellar medium (ISM), we calculated the decorrelation bandwidth ($\approx \frac{1}{2\pi\tau}$) to be 12 kHz. This value is smaller than the frequency resolution (390 kHz) of our data set, indicating that scintillation from the ISM is unlikely to be responsible for the observed magnification. Therefore, we interpret this as lensing due to the irregular distribution of the circumstellar plasma plasma around the companion. In regions characterized by strongly varying electron density, radio emission can undergo significant magnification due to plasma lensing. Plasma lensing was observed at only one of the epochs at 400 MHz. There were no simultaneous observations at other frequency bands at that epoch. We did not detect any lensing effects in our other observations at 400 MHz as well as at 650

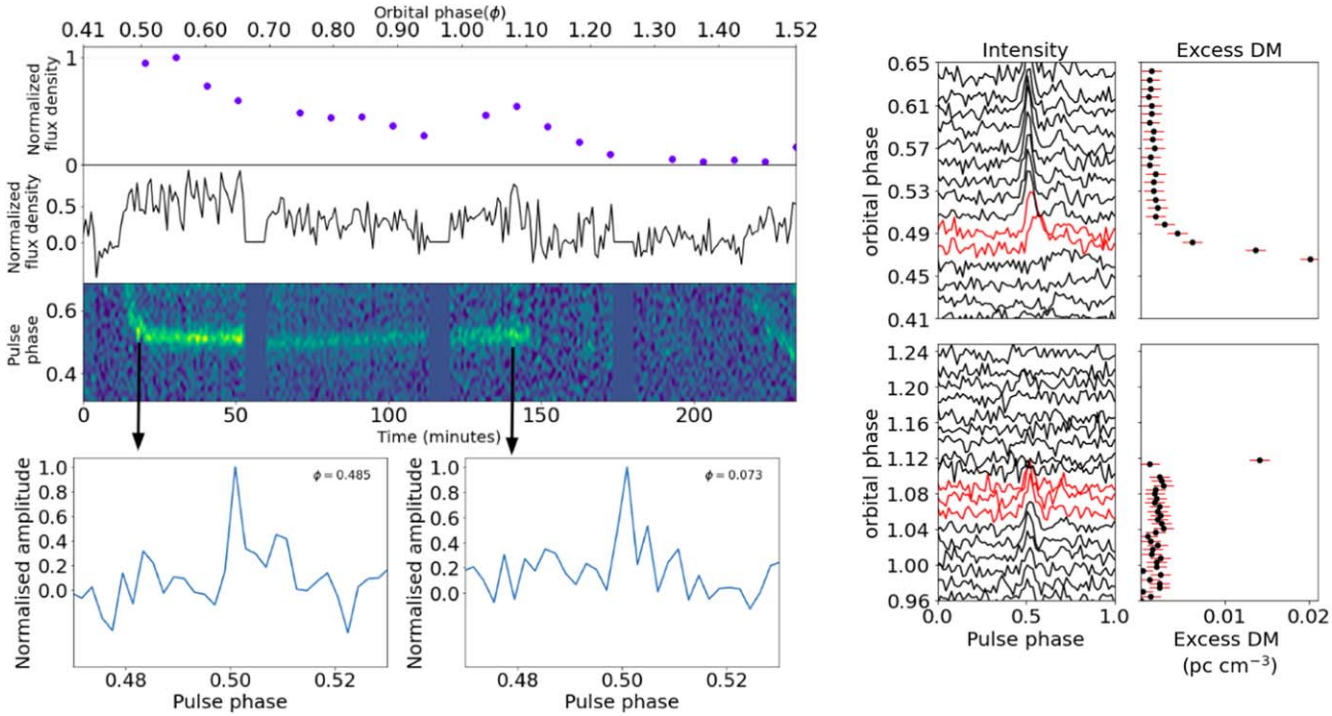

Figure 6. Left panel: enhanced flux density and increase in brightness in pulsed radiation near eclipse boundaries observed with uGMRT at 400 MHz on 2023 December 16 in an observation covering nearly one full orbit (∼3.5 hr) of the pulsar, monitoring the MSP starting from one egress and ending at the next egress. Right panel: total intensity for average pulse profiles of PSR J1908+2105 during the ingress (bottom panels) and egress (upper panels) of the eclipse from uGMRT observations at 400 MHz. The red lines are the last and first pulses before and after the eclipse. The pulse profiles near the eclipse become wider. The corresponding DM (black dots) variations of the eclipse are shown in the right panels. The red bars are the errors on the DM.

and 2368 MHz. We note that multiple plasma lenses may or may not form within a compact region capable of focusing at vastly different frequencies due to the frequency-dependent scaling of dispersive and geometric delays (R. Main et al. 2018). Moreover, the turbulence and density gradients in the eclipse medium responsible for lensing are random and can vary widely between the observing epochs. Instances of extreme plasma lensing have been observed surrounding eclipses in two other eclipsing spider pulsars: the BW MSP B1957+20 (R. Main et al. 2018) and the RB MSP B1744−24A (A. V. Bilous et al. 2019). These lensing effects result in highly magnified pulses, amplifying their intensity by up to 10 times compared to those from the noneclipse region, with this enhancement lasting for tens of milliseconds. In PSR B1957+20, R. Main et al. (2018) reported a magnification factor of nearly 40 during lensing events. Similarly, A. V. Bilous et al. (2019) observed an amplification factor of 10 compared to the pulses from the noneclipse region in PSR B1744−24A. Unlike R. Main et al. (2018), we do not observe any bright structures in the dynamic spectra. This may be due to the presence of multiple lenses in the eclipse outflow creating an interference pattern among the lensing images and dissolving any distinct features. The lensing phenomenon resolves the pulse emission, thereby constraining emission sizes and component separations. It can also be used to infer the velocity of the eclipsing outflow. Following R. Main et al. (2018), A. V. Bilous et al. (2019), and J. M. Cordes et al. (2017), we tried to constrain the characteristic size of a 1D lens. For $\nu = 400$ MHz, the Fresnel scale at the lens plane is found to be

$$r_F \approx \sqrt{\frac{c d_{\rm sl} d_{\rm lo}}{\nu d_{\rm so}}} \approx 26 \times \sqrt{d} \ \ {\rm km}, \tag{4}$$

where, we assume, $d_{\rm sl}$ is the distance to the lens from source $\approx d \times a$ ($a\approx$ orbital separation between the pulsar and the companion $\approx 1.30\, R_\odot$); $d_{\rm lo}$ is the distance to the lens from the observer; and $\approx d_{\rm so}$ is the distance to the source from the observer ≈ 2.6 kpc. We define the size of the lens, $R_{\rm lens} \approx R \times a$. From J. M. Cordes et al. (2017), we find the amplification due to lensing:

$$G \sim \frac{R_{\rm lens}}{r_F} \approx 3.4 \times 10^4 \frac{R}{\sqrt{d}}. \tag{5}$$

As the maximum gain, $G \approx 4$:

$$\frac{R}{\sqrt{d}} \approx 1.15 \times 10^{-4}. \tag{6}$$

The time of caustic crossing (Equation (22) of J. M. Cordes et al. 2017) is given by

$$t_c \sim \frac{R_{\rm lens}\, \delta G/G}{v_{\rm trans}\, G^2} \left(\frac{d_{\rm lo}}{d_{\rm so}}\right) \approx 132 \times R \ \ {\rm s}, \tag{7}$$

where $v_{\rm trans}$ is the relative velocity between the pulsar and companion outflow and can be approximated to the orbital velocity of the companion $\approx 428\ {\rm km\ s^{-1}}$ (M. Tavani & L. Brookshaw 1991, 1993). We assume the fractional gain $\delta G/G \approx 4/4 \approx 1$. Therefore, for $t_c \sim$ 1–50 ms, we obtain

$R \approx 7.5 \times 10^{-6}$–$3.7 \times 10^{-4}$ km. Hence, the corresponding $R_{\rm lens} \approx 6.8$–343 km and $d \approx 0.004$–10.4. From the obtained value of d, we can assume the lens material is located very near to the companion that is at an orbital separation a. Therefore, the resolution of the lens for given magnification $G \sim 1.9R_1/G^{1/2}$ for the linear lens and $1.9R_1/G^{1/4}$ for a circular lens (R. Main et al. 2018), where $R_1 = \curlywedge \approx 15$ km for our observing length $\lambda = 75$ cm. The resulting resolution is 14.3 km for the linear lens and 20 km for the circular lens, both of which are significantly smaller than the light-cylinder radius of PSR J1908+2105 ($R_{\rm LC} = cP/2\pi \approx 122$ km). This makes lensing highly effective for probing the emission geometry.

4. Eclipse Mechanisms

In the following section, we have applied the eclipse mechanism proposed by C. Thompson et al. (1994) to PSR J1908+2105 to explore the potential causes of the observed eclipsing. Figure 6 represents the total intensity and excess DM near the eclipse ingress and egress at 400 MHz. The eclipse is centered around orbital phase 0.28 at this frequency with a duration of ∼80 minutes, i.e., nearly 38% of the orbit. The radius of the companion's Roche lobe, R_L, is estimated by assuming a binary inclination of 90° and using the following equation from P. P. Eggleton (1983):

$$R_L = \frac{0.49aq^{2/3}}{0.6q^{2/3} + ln(1 + q^{2/3})} \sim 0.21R_{\odot}, \quad (8)$$

where the mass ratio of the companion to the pulsar, denoted as $q = m_c/m_p$, and the separation between them, a ($\sim 1.3\,R_{\odot}$). The obscured portion of the companion's orbit extends to $1.48\,R_{\odot}$, significantly larger than that of the Roche lobe radius. This indicates that the material causing the eclipse is located well outside the companion's Roche lobe, implying it is not gravitationally bound to the companion.

Since the eclipse weakens at higher frequencies, we can probe deeper into the eclipse medium at these frequencies. We found the maximum electron column density at 2368 MHz to be $N_e \sim 1.78 \times 10^{18}\,{\rm cm}^{-2}$. However, due to the complete eclipse, only a lower limit on the electron column density could be determined near the egress. From this, we derive an electron volume density of $n_e \sim 1.1 \times 10^7\,{\rm cm}^{-3}$, where $n_e = N_e/L$, and L is the absorption length of the eclipse medium at 2368 MHz $\sim 2.3\,R_{\odot}$.

We have ruled out plasma frequency cutoff as the primary eclipse mechanism, as the plasma frequency is determined to be $f_p = 8.5(\frac{n_e}{\rm cm^{-3}})^{1/2}$ kHz ∼ 28.35 MHz, significantly lower than the observed cutoff frequency (>4000 MHz). Refraction is also excluded as a major mechanism since refraction would require pulse delays in the range of 10–100 ms, whereas we observed a delay of 445 μs at 2368 MHz near the eclipse boundary.

A scattering of radio waves could cause an eclipse if the pulse broadens beyond the pulsar period. However, the scattering timescales at 1200 and 400 MHz (Section 3.1) are significantly shorter than the pulsar spin period (<2.56 ms). We found that the scattering timescales are similar in the eclipse phase and the noneclipse phase. The observed scattering timescale near eclipse ingress is found to be 0.09 and 0.06 ms at 400 MHz and 2 GHz, respectively; whereas in the noneclipse phase, we calculate a scattering timescale of 0.08 ms and 0.05 ms, making scattering an unlikely explanation for the observed eclipsing.

We also considered whether free–free absorption could account for frequency-dependent eclipsing. For free–free absorption to be the cause, the optical depth τ_{ff} (given by Equation (11) of C. Thompson et al. 1994) must exceed 1. Using $\tau_{ff} > 1$, we derived the condition $T \leqslant 42 \times f_{cl}^{2/3}$ K, where T is the temperature and $f_{\rm cl}$ is the clumping factor. For significant free–free absorption across both high and low frequencies, either a very low temperature or a very high clumping factor would be required. However, neither condition is physically feasible: the temperature of stellar wind (10^8–10^9 K) is well above the necessary threshold, and an extremely high clumping factor is not plausible in the eclipse environment (C. Thompson et al. 1994).

Induced Compton scattering is also ruled out as a major eclipse mechanism, as the calculated optical depth (using Equation (26) from C. Thompson et al. 1994) is less than 1. The optical depth for induced Compton scattering, estimated with a mean flux density of 0.22 ± 0.01 mJy, a pulsar spectral index of $\alpha = -1.9$, a companion distance of approximately 1.3 solar radii, and a pulsar distance of 3.05 kpc (derived from the DM of the pulsar using NE2000 and YMW16 models, averaging the estimates of 2.6 kpc and 3.2 kpc), is too low to account for the observed eclipse.

We also explored whether cyclotron absorption could explain the observed eclipse. We calculated the characteristic magnetic field (B_E) in the eclipse medium to be 16 G. The calculated cyclotron frequency, $\nu_B = \frac{eB}{2\pi m_e c}$, is 44 MHz, where m_e is the mass of the electron, e is the charge on the electron, and c is the speed of light. Therefore, the corresponding cyclotron harmonic, m, at the observing frequency ν can be calculated using $m = \frac{\nu}{\nu_B}$. According to Equation (43) from C. Thompson et al. (1994), the temperature within the eclipse medium needs to be approximately 1.5×10^8 K for cyclotron absorption to occur at 400 MHz. However, the validity of the cyclotron approximation holds for temperatures $T \leqslant 3.9 \times 10^6$ K at 400 MHz. At a higher frequency of 2368 GHz, the required temperature for cyclotron absorption reduces to 6.1×10^7 K, but cyclotron approximation is valid for only $T \leqslant 1.9 \times 10^4$ K at 2368 MHz. Thus, cyclotron absorption is not the predominant mechanism explaining the observed eclipses across all frequencies.

However, according to C. Thompson et al. (1994), absorption by thermal electrons dominates at lower cyclotron harmonics. As we move toward the higher harmonic, synchrotron absorption by the transrelativistic nonthermal free electrons become significant, and therefore, it can be thought of as a major eclipse mechanism at higher frequencies. S. Kumari et al. (2024a) and D. Kansabanik et al. (2021) found that synchrotron absorption can also explain the frequency-dependent nature of the eclipse. Therefore, we investigated the possible mechanism for the eclipse observed at unusually high frequencies for PSR J1908+2105, focusing on synchrotron absorption as the major eclipse mechanism. Our goal was to determine what is different in the eclipse medium of this system compared to other known spiders, leading to such high-frequency eclipses. The energy density distribution of the nonthermal electrons for synchrotron absorption is ($n(E) = n_0 E^{-p}$), where p is the power-law index and n_o is the nonthermal electron density, which is assumed to be 1% of the total electron density (n_e). The optical depth for synchrotron

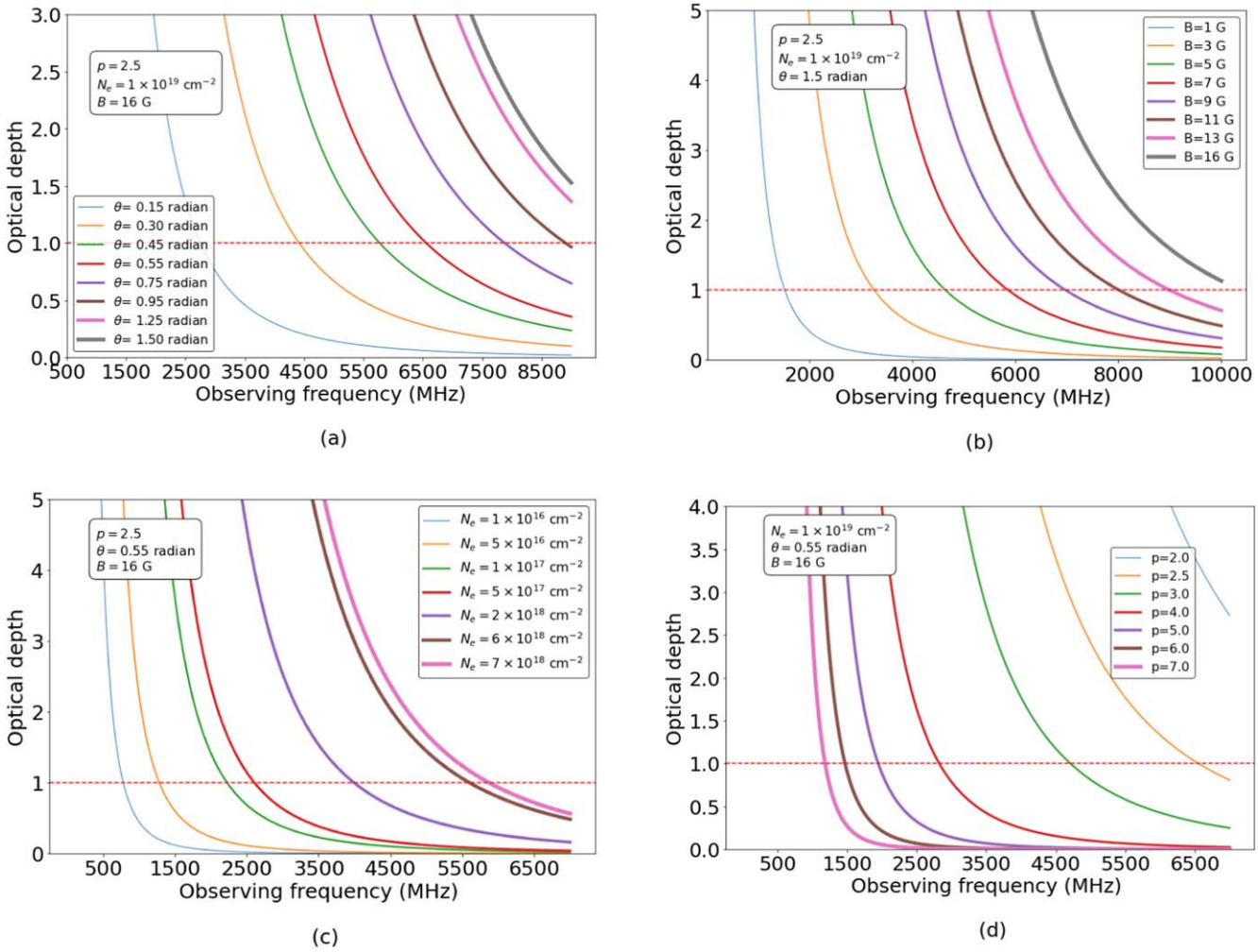

Figure 7. Simulation of optical depth variation with frequency through changes in viewing angle (θ) (a), magnetic field (B) (b), electron density (N_e) (c), and electron power-law index (p) (d) in the eclipse medium for PSR J1908+2105. The axis ranges were selected to enhance the plot's clarity and provide a better explanation of optical depth variation as we vary different parameters.

absorption is given by

$$\tau_{\rm syn} = \left(\frac{3^{\frac{(p+2)}{2}}\Gamma(\frac{3p+2}{12})\Gamma(\frac{3p+22}{12})}{4}\right)\left(\frac{\sin\theta}{m}\right)^{\frac{p+2}{2}}\frac{n_0 e^2}{m_e c\nu}L, \qquad (9)$$

where θ is the angle between the magnetic field lines at the eclipse medium and our line of sight, and L is the absorption length. Figure 7 illustrates the optical depth in the eclipse medium depending on the parameters p, θ, N_e, and B. We can see that the optical depth and, therefore the eclipse cutoff frequency, can vary if we change any of these four parameters,[6] and therefore, constraining these parameters accurately for a particular system by removing the degeneracy is almost impossible. However, the observed eclipse at a frequency >4 GHz for PSR J1908+2105 helps us to get a better constraint and put a limit on these parameters, N_e, B, p, and θ. In Table 3, we have compared the maximum electron density and corresponding eclipse cutoff frequency found for a few of the spider systems, for which a detailed eclipse study has been done. MSPs exhibiting eclipses at higher frequencies tend to have higher electron densities compared to those with lower eclipse cutoff frequencies. Notably, MSPs that exhibit eclipses at frequencies greater than 3 GHz have an electron density (N_e) of approximately 10^{18} cm^{-2} at the eclipse boundary, which is an order of magnitude higher than the electron density found at the center of the eclipse medium for other eclipsing spiders. Therefore, higher electron density in the eclipse medium can be one reason for the observed high-frequency eclipse for PSR J1908+2105. Thus, we infer higher electron column density can play a major role in deciding the eclipse cutoff frequency of frequency-dependent eclipsing. Optical depth for Compton scattering at the cutoff frequency (also presented in Table 3) ranges from 10^{-5} to 10^{-2}, indicating that this mechanism may not be a major contributor to eclipsing at higher frequencies.

For absorption by nonthermal electrons to occur, the electron power-law index can vary from 2 to 7 for the range of cyclotron harmonic numbers, $m = \frac{\nu}{\nu_B} \approx 10$–$100$, and viewing angle ($\theta$) from 20° to 80° (G. A. Dulk & K. A. Marsh 1982). For absorption by nonthermal, mildly relativistic electrons, this value of electron power-law index converges between 2 to 3 as shown with the numerical calculation by T. Takakura & E. Scalise (1970) and R. Ramaty (1969). Therefore, to

[6] https://github.com/Rimi98/eclipse_mechanism

Table 3
Maximum Electron Column Density and Eclipse Cutoff Frequency for Spider MSPs

MSP	N_e Maximum (cm^{-2})	Cutoff Frequency (ν_c) (MHz)	τ_{ind}[d]	References
J0024−7204J[a]	5×10^{16}	<734	1.29×10^{-3}	(6)
J1023+0038[a]	4.6×10^{17}	∼3000	1.12×10^{-4}	(1), (2)
J1227−4853[b]	2.4×10^{17}	$750 < \nu_c < 1400$	7.6×10^{-5}	(7)
J1431−4715[a]	9.0×10^{17}	∼1251	1.98×10^{-5}	(6)
J1544+4937[a]	3.0×10^{16}	$338 < \nu_c < 558$	4×10^{-2}	(5)
J1731−1847[a]	3.0×10^{18}	>3000	3.96×10^{-4}	(2)
J1748−2446A[a]	2.0×10^{18}	$1600 < \nu_c < 2600$	7.90×10^{-3}	(2), (3)
J1810+1744[b]	3.0×10^{16}	>850[c]	6.66×10^{-4}	(8), (11)
J1816+4510[b]	3.0×10^{17}	>1400[c]	4.94×10^{-5}	(8), (9)
J1908+2105[b]	2.0×10^{18}	>4000	1.85×10^{-3}	This work
J1959+2048[b]	4.0×10^{17}	>1400[c]	6.43×10^{-5}	(2), (6), (10)
J2051−0827[a]	4.0×10^{17}	∼1000	5.91×10^{-4}	(2), (4)

Notes. MSPs listed in bold are those that exhibit eclipses at frequencies above 3 GHz.
[a] Electron density at the center of the eclipse medium.
[b] Electron density at the eclipse boundary.
[c] Cutoff frequency is not reported due to band-limited spectra above 1.4 GHz.
[d] Optical depth for Compton scattering at the cutoff frequency was calculated using Equation (26) from C. Thompson et al. (1994) using the parameters from the corresponding references and the ATNF pulsar catalog (R. N. Manchester et al. 2005).
References. (1) A. M. Archibald et al. (2009), (2) S. D. Bates et al. (2011), (3) X. P. You et al. (2018), (4) B. W. Stappers et al. (2001), (5) S. Kumari et al. (2024a), (6) S. Kumari et al. (2024b), (7) S. Kudale et al. (2020), (8) E. J. Polzin et al. (2020), (9) K. Stovall et al. (2014), (10) M. F. Ryba & J. H. Taylor (1991), (11) E. J. Polzin et al. (2018).

constrain the viewing angle θ for our observed high-frequency eclipse, we have kept the $p = 2.5$ and taken the magnetic field in the eclipse medium $B = 1$ G as we obtained in Section 3.5 and predicted electron density at the eclipse medium $N_e = 1 \times 10^{19}$ and varied θ from 0.15 rad to 1.50 rad (D. Kansabanik et al. 2021). It can be seen in panel (a) of Figure (7) that θ should be >0.30 rad for the eclipse to occur at >4 GHz.

Next, we set $p = 2.5$ and used the predicted maximum electron column density at the eclipse center, $N_e = 1 \times 10^{19}\,cm^{-2}$. Assuming the magnetic field is perpendicular to the line of sight (i.e., $\theta = 1.5$ rad), we varied the magnetic field (B) from 1 Gauss to 16 Gauss. This analysis suggests that the lower limit of the magnetic field in the eclipse medium must be $\geqslant$5 Gauss to account for the observed eclipse (see panel (b), Figure 7).

Although it is already evident, we can see in panel (c) of Figure 7 that, keeping $p = 2.5$, $B = 16$ Gauss and $\theta = 0.55$ rad fixed, the eclipse cutoff frequency shifts toward higher frequency as we increase the electron density.

Lastly, keeping $N_e = 1 \times 10^{19}\,cm^{-2}$, $B = 16$ Gauss, and $\theta = 0.55$ rad fixed, we can see that, for the eclipse to occur at frequency >4 GHz, the electron power-law index (p) for synchrotron absorption should be $3 < p < 2$ (panel (d), Figure 7), suggesting major eclipse mechanism to be absorption by nonthermal transrelativistic electrons (R. Ramaty 1969; T. Takakura & E. Scalise 1970).

Using a similar approach and considering the reported N_e, we determined that the minimum magnetic field required to explain the observed eclipse cutoff at 3 GHz for PSR J1023+0038 is 10 Gauss, with an upper limit of 200 Gauss. For PSR J1431−4715, the minimum magnetic field needed for an eclipse cutoff at 1.2 GHz is 2 Gauss, with a maximum limit of 35 Gauss. Similarly, for PSR J2051−0827, the required magnetic field for the eclipse cutoff at 1 GHz ranges from a minimum limit of 2 Gauss to a maximum limit of 50 Gauss.

Therefore, we have inferred that synchrotron absorption by free electrons is the primary mechanism responsible for the observed eclipses in PSR J1908+2105.

5. Summary

This study of the spider MSP J1908+2105 significantly advances our understanding of the magnetic properties within the eclipse medium of spider MSPs, shedding light on the dynamics of these extreme binary systems. PSR J1908+2105 stands out as a unique system that blurs the lines between "BWs" and "RBs." Its short orbital period, low companion mass, and extensive eclipses characterize it as an atypical "spider" variant, sharing traits of both subclasses. Notably, it exhibits unusual eclipses over 30% of its orbit at frequencies exceeding 4 GHz. The other two MSPs exhibiting eclipses above 3 GHz are PSR J1723−2837 and PSR J1731−1847. PSR J1723−2837, which falls into the RB category, has a companion mass ranging from 0.4 to 0.7 $M_\odot$. PSR J1731−1847, with a companion mass of 0.043 $M_\odot$, is classified as a BW.

We explain the trailing material observed at the eclipse boundaries by modeling the electron density distribution around companion stars. The linear depolarization and increased RM near the eclipse medium suggest a higher electron density and magnetic field, approaching closer to the companion. While extensive eclipses above 4 GHz have been observed in three spider MSPs, detailed studies for the other two are lacking.

For PSR J1908+2105, our wide-bandwidth observations identify synchrotron absorption as the primary eclipse mechanism, allowing us to establish a minimum required magnetic field for eclipses at such high frequencies. We also found a correlation between eclipse cutoff at higher frequencies and increased electron density. The emission geometry, constrained from the observed position angle (i.e., PPA) swing, has been characterized in only a few spider MSPs.

Additionally, we observed lensing effects in uGMRT band 3 near eclipse boundaries causing enhanced flux density and brightness. These findings provide crucial insights into the complex interactions within spider MSP systems, offering a more comprehensive understanding of the eclipse mechanisms and magnetic environments that define these intriguing binaries.

Acknowledgments

We acknowledge the support of the Department of Atomic Energy, Government of India, under project No. 12-R&D-TFR5.02-0700. The GMRT is run by the National Centre for Radio Astrophysics of the Tata Institute of Fundamental Research, India. We acknowledge the support of GMRT telescope operators for observations. The Parkes radio telescope is part of the Australia Telescope which is funded by the Commonwealth of Australia for operation as a National Facility managed by CSIRO. We sincerely thank the reviewer for valuable feedback and insightful suggestions that improved the clarity and presentation of this work.

ORCID iDs

Ankita Ghosh https://orcid.org/0009-0002-3211-4865
Bhaswati Bhattacharyya https://orcid.org/0000-0002-6287-6900
Sangita Kumari https://orcid.org/0000-0002-3764-9204
Simon Johnston https://orcid.org/0000-0002-7122-4963
Patrick Weltevrede https://orcid.org/0000-0003-2122-4540
Jayanta Roy https://orcid.org/0000-0002-2892-8025

References

Archibald, A. M., Stairs, I. H., Ransom, S. M., et al. 2009, Sci, 324, 1411
Bates, S. D., Bailes, M., Bhat, N. D. R., et al. 2011, MNRAS, 416, 2455
Bhat, N. D. R., Cordes, J. M., Camilo, F., Nice, D. J., & Lorimer, D. R. 2004, ApJ, 605, 759
Bilous, A. V., Ransom, S. M., & Demorest, P. 2019, ApJ, 877, 125
Cordes, J. M., Wasserman, I., Hessels, J. W. T., et al. 2017, ApJ, 842, 35
Cromartie, H. T., Camilo, F., Kerr, M., et al. 2016, ApJ, 819, 34
Crowter, K., Stairs, I. H., McPhee, C. A., et al. 2020, MNRAS, 495, 3052
Deneva, J. S., Ray, P. S., Camilo, F., et al. 2021, ApJ, 909, 6
Dulk, G. A., & Marsh, K. A. 1982, ApJ, 259, 350
Eggleton, P. P. 1983, ApJ, 268, 368
Fruchter, A. S., Stinebring, D. R., & Taylor, J. H. 1988, Natur, 333, 237
Ghosh, A., Bhattacharyya, B., Lyne, A., et al. 2024, ApJ, 965, 64
Gupta, Y., Ajithkumar, B., Kale, H. S., et al. 2017, CSci, 113, 707
Hobbs, G., Manchester, R. N., Dunning, A., et al. 2020, PASA, 37, e012
Hobbs, G. B., Edwards, R. T., & Manchester, R. N. 2006, MNRAS, 369, 655
Hotan, A. W., van Straten, W., & Manchester, R. N. 2004, PASA, 21, 302
Kansabanik, D., Bhattacharyya, B., Roy, J., & Stappers, B. 2021, ApJ, 920, 58
Kudale, S., Roy, J., Bhattacharyya, B., Stappers, B., & Chengalur, J. 2020, ApJ, 900, 194
Kumari, S., Bhattacharyya, B., Sharan, R., et al. 2024a, ApJ, 961, 155
Kumari, S., Bhattacharyya, B., Sharan, R., et al. 2024b, ApJ, 973, 19
Li, D., Lin, F. X., Main, R., et al. 2019, MNRAS, 484, 5723
Lin, F. X., Main, R. A., Jow, D., et al. 2023, MNRAS, 519, 121
Lin, F. X., Main, R. A., Verbiest, J. P. W., Kramer, M., & Shaifullah, G. 2021, MNRAS, 506, 2824
Main, R., Yang, I. S., Chan, V., et al. 2018, Natur, 557, 522
Manchester, R. N., Hobbs, G. B., Teoh, A., & Hobbs, M. 2005, AJ, 129, 1993
Polzin, E. J., Breton, R. P., Bhattacharyya, B., et al. 2020, MNRAS, 494, 2948
Polzin, E. J., Breton, R. P., Clarke, A. O., et al. 2018, MNRAS, 476, 1968
Polzin, E. J., Breton, R. P., Stappers, B. W., et al. 2019, MNRAS, 490, 889
Radhakrishnan, V., & Cooke, D. J. 1969, ApL, 3, 225
Ramaty, R. 1969, ApJ, 158, 753
Reddy, S. H., Kudale, S., Gokhale, U., et al. 2017, JAI, 6, 1641011
Roberts, M. S. E. 2013, in IAU Symp. 291, Neutron Stars and Pulsars: Challenges and Opportunities after 80 years, ed. J. van Leeuwen (Cambridge: Cambridge Univ. Press), 127
Ryba, M. F., & Taylor, J. H. 1991, ApJ, 380, 557
Stappers, B. W., Bailes, M., Lyne, A. G., et al. 2001, MNRAS, 321, 576
Stovall, K., Lynch, R. S., Ransom, S. M., et al. 2014, ApJ, 791, 67
Swarup, G. 1991, in ASP Conf. Ser. 19, IAU Colloq. 131: Radio Interferometry. Theory, Techniques, and Applications, ed. T. J. Cornwell & R. A. Perley (San Francisco, CA: ASP), 376
Takakura, T., & Scalise, E. 1970, SoPh, 11, 434
Tavani, M., & Brookshaw, L. 1991, ApJL, 381, L21
Tavani, M., & Brookshaw, L. 1993, A&A, 267, L1
Thompson, C., Blandford, R. D., Evans, C. R., & Phinney, E. S. 1994, ApJ, 422, 304
van Straten, W. 2004, ApJS, 152, 129
Wang, S. Q., Wang, J. B., Li, D. Z., et al. 2023, ApJ, 955, 36
You, X. P., Manchester, R. N., Coles, W. A., Hobbs, G. B., & Shannon, R. 2018, ApJ, 867, 22